

Straightening the Ruler: Field-Level Inference of the BAO Scale with LEFTfield

Ivana Babić,^a Fabian Schmidt,^a Beatriz Tucci^a

^aMax-Planck-Institut für Astrophysik, Karl-Schwarzschild-Straße 1, 85748 Garching, Germany

E-mail: ibabic@mpa-garching.mpg.de, fabians@mpa-garching.mpg.de, tucci@mpa-garching.mpg.de

Abstract. Current inferences of the BAO scale from galaxy clustering employ a reconstruction technique at fixed cosmology and bias parameters. Here, we present the first consistent joint Bayesian inference of the isotropic BAO scale, jointly varying the initial conditions as well as all bias coefficients, based on the EFT-based field-level forward model LEFTfield. We apply this analysis to mock data generated with a much higher cutoff (resolution), resulting in a significant model mismatch between mock data and the model used in the inference. We demonstrate that the remaining systematic bias in the BAO scale is below 2% for all data considered and below 1% when Eulerian bias is used for inference. Furthermore, we find that the inferred error on the BAO scale is up to 1.6 times smaller compared to that from a replication of the standard power-spectrum reconstruction approach, using the same scales as in the field-level inference, with the improvement growing towards smaller scales (higher k). Thus, a field-level approach to BAO not only allows for a consistent inference of the BAO scale, but promises to achieve more precise measurements on the same data as well.

Contents

1	Introduction	1
2	Forward Model	3
3	Code Implementation	7
4	Synthetic Data sets	8
5	Field level BAO inference	8
5.1	Sampling method and data analysis	8
5.2	Field-level results	9
6	Comparing the field-level results to the reconstruction approach	12
6.1	BAO Reconstruction Procedure	12
6.2	Inference results and comparison with the field level	16
7	Discussion and Conclusions	16
A	Data Analysis	19
A.1	Correlation length	19
A.2	Parameter posteriors: marginalized likelihood	19
A.3	Parameter posteriors: non-marginalized likelihood	20

1 Introduction

Baryon Acoustic Oscillations (BAO) represent one of the most significant observables in cosmology. Originating from the period when photons and baryons were tightly coupled, the imprints of BAO are visible in both the Cosmic Microwave Background (CMB) temperature anisotropies and the clustering of matter at later times. By measuring the apparent size of the BAO scale, r_s , in the late-time matter distribution, it is possible to estimate both the angular diameter distance and the Hubble parameter as functions of redshift. Moreover, the BAO feature imprinted in galaxy clustering is much less sensitive to the details of the galaxy-matter relation (bias) than the broad-band galaxy statistics. However, the nonlinear evolution of the matter density field and the formation of structures complicate this picture. The bulk motion of matter (and galaxies with it) leads to a damping of the BAO oscillations in the power spectrum, reducing the accuracy with which the BAO scale can be measured from the late-time clustering of galaxies [1–4].

Traditional BAO inference methods attempt to correct for the bulk flows by performing a nonlinear transformation of the data. Central to this is the estimation of displacements from the observed density field to move galaxies to their estimated initial positions [5–14]. This method does require making assumptions about cosmology and bias, and for a consistent inference one should really sample the parameters associated with these together with the BAO scale. Here, we aim to deal with this issue by adopting a fully Bayesian field-level forward modeling approach. This approach incorporates BAO reconstruction by jointly inferring the large-scale modes responsible for the bulk flow [15]. Crucially, it does not rely on

a fiducial cosmology, as usually assumed in the reconstruction procedure. Instead, cosmological parameters are jointly and consistently inferred with the initial conditions and bias parameters.¹ Furthermore, since the field-level approach does not rely on compression functions, but instead obtains the information directly from the field, it also extracts the BAO information contained in higher n -point functions such as the bispectrum.

We have already discussed these issues in our previous work [16] where the field-level approach for inferring the BAO scale was first introduced. The starting point is the joint posterior for the initial density field, cosmological parameters, and nuisance parameters, which include bias parameters and stochastic amplitudes. At the heart of the field-level posterior lies the likelihood function, which is the key ingredient allowing us to access the information at the field level. The likelihood we use was derived within the framework of the effective field theory (EFT) of large scale structure (LSS) [17, 18] in a series of papers [15, 19, 20] and we will refer to it as the EFT likelihood or field-level likelihood. In every EFT theory, a fundamental component is the cutoff scale, denoted as Λ , representing the maximum wavenumber of modes considered in the calculations (in n -point-function-based analyses, this is often denoted with k_{max}). While the specific value of Λ is arbitrary, the upper limit for Λ in the case of the EFT of LSS is the nonlinearity scale ($\Lambda_{\text{NL}} \approx 0.25 h \text{Mpc}^{-1}$ at $z = 0$), where perturbation theory of LSS breaks down. In addition to the BAO scale, EFT-based field-level inference results have been applied to the σ_8 parameter in [21–24] as well as the growth rate f in [25].

In our previous paper on BAO [16], we analyzed dark matter halo samples in N-body simulations, but in the scenario of fixed initial conditions. To assess the effectiveness of the field-level approach combined with the EFT likelihood, we compared it to a power spectrum likelihood whose covariance was derived to account for the fixed initial conditions (i.e., no cosmic variance). Our analysis revealed that the error bars for the BAO scale were between 1.1 and 3.3 times smaller when using the field-level likelihood as compared to the power spectrum without BAO reconstruction, where this range corresponds to the range of scales considered, $\Lambda = [0.1 - 0.25] h \text{Mpc}^{-1}$, as well as different halo samples and redshifts.

In this paper, we go a significant step further and use the field-level likelihood to perform a joint inference of the BAO scale and the initial conditions, which of course is necessary in the application to real data. Sampling initial conditions is challenging since the dimensionality of the parameter space is of the order of $10^5 - 10^6$. To deal with this challenge, we follow the lead of [26] and use the Hamiltonian Monte Carlo (HMC) [27] sampling method to sample the initial conditions and slice sampler [28] to sample the cosmological parameters. We apply this analysis to mock data generated with the `LEFTfield` code, a Lagrangian EFT-based forward model [29], which we also use for the inference. Importantly, our mock data are generated with a substantially higher cutoff than that used in the inference, as well as different bias models (with bias parameters representative of actual halo samples), so that we can test the robustness against model mis-specifications.

In a pioneering work, Ref. [30] demonstrated field-level inference of cosmology and distances on mock data, obtaining very tight constraints on the expansion history. Differently to this work, however, they did not separate BAO and broad-band (Alcock-Paczyński distortion) contributions. In addition, our forward model differs substantially, in that we use an EFT-based forward model, and, crucially, our results also incorporate model mis-specification.

¹Note that in this work, we also fix all cosmological parameters apart from the BAO scale in the inference, but all bias parameters including the linear bias b_1 are jointly inferred with the BAO scale.

Apart from demonstrating the feasibility and robustness of BAO scale inference at the field level with `LEFTfield`, the second main goal of this work is to quantify the information gain relative to the standard reconstruction algorithm [31]. To this end, we adapt the reconstruction pipeline to deal with our mock data, and then perform an inference using, as closely as possible, the same cutoffs and scales as used in the field-level inference. This allows us to perform a consistent comparison of the two methods. The results of this comparison are presented in Sec. 6.2.

In Section 2, we briefly introduce the forward model used in this paper. Section 3 provides details of the implementation within the `LEFTfield` code. Section 4 elaborates on the generation of mock data. Finally, in Section 5.2, we present the results from the joint inference of BAO along with the initial conditions, and compare to the power-spectrum analysis with and without reconstruction applied in Section 6.

2 Forward Model

The idea of forward modeling is to start from the initial conditions and then model the tracer overdensity field δ_g at late times. The latter is defined as

$$\delta_g(\mathbf{x}, \tau) \equiv \frac{n_g(\mathbf{x}, \tau)}{\bar{n}_g(\tau)} - 1 = \delta_{g,\text{det}}(\mathbf{x}, \tau) + \epsilon(\mathbf{x}, \tau), \quad (2.1)$$

where τ is the conformal time, $n_g(\mathbf{x}, \tau)$ is the comoving rest-frame tracer density and $\bar{n}_g(\tau)$ is its position-independent mean. $\delta_{g,\text{det}}(\mathbf{x}, \tau)$ is the deterministic part predicted by the forward model and $\epsilon(\mathbf{x}, \tau)$ is the stochastic (noise) contribution.

The forward model employed here was introduced in [15]. The main object of this model is a joint posterior for the initial density field δ_{in} , cosmological parameters θ and “nuisance” parameters (bias parameters $\{b_O\}$ and stochastic amplitudes σ) given the data, i.e. $P(\delta_{\text{in}}, \theta, \{b_O\}, \sigma | \delta_g)$. There are four ingredients to this posterior:

- Prior on the initial conditions
- Forward model for matter and gravity
- Bias model
- Likelihood.

We will elaborate more on each of them in the following sections, but for now, let us emphasize our usage of the EFT of LSS. Relying on the EFT approach means that we have a natural occurrence of a cutoff scale Λ . While in analytical loop calculations one typically sends this cutoff to infinity for convenience, it is necessary to keep it finite when using a field-level forward model [21], in close analogy to lattice field theory (see [32] for a discussion of the connection between both conventions). Thus, in our case Λ denotes the maximum wave number included in the analysis, and Λ is restricted to be smaller than the nonlinearity scale at which the EFT of LSS breaks down. In practice, the cutoff Λ_{in} is applied in the initial conditions (i.e., *in the free field*), as well as in the likelihood evaluation in order to only include the modes in the data that are below the cutoff $k_{\text{max}}^{\text{like}}$; specifically, throughout this paper we keep $\Lambda_{\text{in}} = k_{\text{max}}^{\text{like}} = \Lambda$.

Initial density field

A single realization of the initial density field is of the form

$$\delta_{\text{in}}(\mathbf{k}, \hat{s}) = W_{\Lambda}(k) \sqrt{P_{\text{L}}(k)} \hat{s}(\mathbf{k}), \quad (2.2)$$

where $W_{\Lambda}(k)$ is a sharp- k filter which we use to ensure the proper renormalization of the evolution of large-scale modes, P_{L} is the linear power spectrum and $\hat{s}(\mathbf{k})$ is the unit Gaussian field which we use to represent the normalized initial conditions (sometimes loosely referred to as “phases”).

Changing the size of the BAO scale

In standard practice, the BAO method is employed to estimate the angular diameter distance to a given observed redshift. Precisely, one compares the predicted scale of the BAO feature to that in the data, while varying the assumed distance. As we have already discussed in [16], this type of approach cannot easily be applied to our setup, since modifying the fiducial distance would result in changes to the comoving volume of the data, and violate the periodic boundary conditions of the simulated catalog. Therefore, we follow a different approach, as described in [16]. Instead of altering distances, we focus on rescaling the predicted comoving sound horizon. Our goal is to change the BAO size in the initial conditions and then perform forward modeling with the modified BAO scale. Since the size of the BAO scale was imprinted into the density field at early times, i.e. where linear theory applies, this is the physically correct way to modify the BAO scale. Importantly, we can keep the comoving volume and boundary conditions of the data unmodified.

To achieve our goal, we start by introducing the parameter β in the standard linear power spectrum approximation,

$$P_{\text{L}}(k, \beta) = P_{\text{L,sm}}(k) [1 + A \sin(k \beta r_{\text{fid}} + \phi) \exp(-k/k_{\text{D}})]. \quad (2.3)$$

Here, $P_{\text{L,sm}}(k)$, A , ϕ , and k_{D} are determined by fitting of Eq. (2.3) to the linear power spectrum obtained using the CLASS code [33]. The parameter r_{fid} signifies the fiducial BAO scale. Additionally, β is defined as the ratio of a proposed BAO scale size r_s to its fiducial size,

$$\beta = \frac{r_s}{r_{\text{fid}}}. \quad (2.4)$$

Changes in β will only affect the oscillatory part of the power spectrum, while the broad-band shape will stay unaffected. Notice that for $\beta = 1$, we recover the fiducial power spectrum.

Next, we introduce the function f^2 as the ratio of the linear power spectrum for the proposed values r_s to the fiducial linear power spectrum,

$$f^2(k, \beta) = \frac{P_{\text{L}}(k, \beta)}{P_{\text{fid}}(k)} = \frac{1 + A \sin(k \beta r_{\text{fid}}) \exp(-k/k_{\text{D}})}{1 + A \sin(k r_{\text{fid}}) \exp(-k/k_{\text{D}})}. \quad (2.5)$$

This allows us to easily find the relationship between proposed and fiducial density field

$$\delta_{\beta}(k, \beta) = f(k, \beta) \delta_{\text{fid}}(k). \quad (2.6)$$

Therefore, the fields $\delta_{\beta}(k, \beta)$ and $\delta_{\text{fid}}(k)$ differ only in the size of the BAO scale; all other parameters are set to the exact same values.

Forward model for matter and gravity

In this paper, we use the Lagrangian perturbation theory (LPT). If we assume that at the initial time $\tau = 0$ the particle was at the position \mathbf{q} , which we call Lagrangian position, then under the gravitational evolution it will move and we will finally observe it at the Eulerian position \mathbf{x} at some time τ . The vector field connecting those two positions is called the Lagrangian displacement field $\boldsymbol{\psi}(\mathbf{q}, \tau)$ and it is the main object of LPT,

$$\mathbf{x}(\mathbf{q}, \tau) = \mathbf{q} + \boldsymbol{\psi}(\mathbf{q}, \tau). \quad (2.7)$$

The evolution of the displacement field is governed by the geodesic equation describing particle trajectories in an expanding universe, coupled with the Poisson equation. To solve these equations, the components of the displacement field are treated as small parameters,

$$\boldsymbol{\psi}(\mathbf{q}, \tau) = \sum_{n=1}^{\infty} \boldsymbol{\psi}^{(n)}(\mathbf{q}, \tau), \quad (2.8)$$

where contributions with higher perturbative order n should be successively suppressed.

One of the key advantages of LPT lies in the possibility to integrate the equations of motion for the displacement field analytically, yielding recursion relations for $\boldsymbol{\psi}^{(n)}$ as a function of $\boldsymbol{\psi}^{(m)}$ with $m < n$. This feature enables a relatively straightforward construction of the displacement field [29, 34–37] (see [38] for a related construction based on Eulerian standard perturbation theory). The starting point of these recursion relations is given by

$$\nabla_q \cdot \boldsymbol{\psi}^{(1)}(\mathbf{q}, \tau) = -\delta^{(1)}(\mathbf{q}, \tau) = -D_{\text{norm}}(\tau)\delta_{\text{in}}(\mathbf{q}), \quad (2.9)$$

where D_{norm} is the normalized growth factor relative to the epoch of the linear power spectrum used in the definition of the initial conditions, Eq. (2.2). The matter density field is given fully nonlinearly by $1 + \delta(x, \tau) = |\mathbf{1} + \nabla_q \boldsymbol{\psi}(q)|^{-1}$. We do not need to evaluate this equation explicitly however, since we instead obtain δ by assigning pseudo-particles to a grid at their Eulerian positions given by Eq. (2.7) (see Sec. 3).

Bias Models

To find a biased tracer density field, we use the deterministic relation

$$\delta_{g,\text{det}} = \sum_O b_O O, \quad (2.10)$$

where O are bias operators and b_O their associated coefficients. At each expansion order, a finite number of operators constitute a basis. The choice of the basis is not unique and we can always alternate between different bases (provided they are complete). In this paper, we focus on the second-order expansion and utilize both Eulerian and Lagrangian bases.

Eulerian Bias

In the case of the Eulerian bias expansion, bias operators are constructed from the matter density field obtained using the LPT as described in the previous section,

$$\delta_{g,\text{det}}(\mathbf{x}, \tau) = \sum_O b_O(\tau) O[\delta_\Lambda](\mathbf{x}, \tau). \quad (2.11)$$

Notice that an additional sharp- k filter is applied to the matter density field δ , putting all its modes with $k > \Lambda$ to zero, before the construction of the bias operators. In this paper, we will use the second order bias expansion including the leading higher-derivative contribution. Bias operators contributing in this case are [39, 40]

$$O \in \{\delta, \delta^2, K^2, \nabla^2 \delta\}, \quad (2.12)$$

where K is the tidal field defined as

$$K^2 \equiv (K_{ij})^2 = \left(\left[\frac{\partial_i \partial_j}{\nabla^2} - \frac{1}{3} \delta_{ij} \right] \delta \right)^2. \quad (2.13)$$

We also include the higher derivative term $\nabla^2 \delta$ which accounts for the non-locality of halo formation. The coefficients of higher-derivative operators are related to the spatial scale R_* which quantifies the size of the spatial region involved in the process of halo formation, and their contribution is suppressed by $k^2 R_*^2$ on large scales.

Lagrangian Bias

In the Lagrangian bias expansion,

$$\delta_{g,\text{det}}^L(\mathbf{q}, \tau) = \sum_{O^L} b_{O^L}(\tau) O^L(\mathbf{q}, \tau), \quad (2.14)$$

the operators O^L are constructed from all scalar contributions to the symmetric part of the tensor $\mathbf{M}(\mathbf{q}, \tau)$, defined as

$$M_{ij}(\mathbf{q}, \tau) \equiv \partial_{q,i} \psi_j(\mathbf{q}, \tau). \quad (2.15)$$

We do not need to include $\text{tr}[M^{(n)}]$ for $n > 1$, as they can always be expressed in terms of scalars constructed using lower-order operators [37]. Here, we again focus solely on the second-order bias expansion. Therefore, the bias operators we use are [40]

$$O^L \in \left\{ \delta, \left(\text{tr} [M^{(1)}] \right)^2, \text{tr} [M^{(1)} M^{(1)}], \nabla^2 \delta \right\}. \quad (2.16)$$

Here, we have replaced $\text{tr}[M^{(1)}]$ with the Eulerian density field δ , which allows for identification of its bias coefficient with the standard linear bias b_δ , commonly referred to as b_1 . We have once again included the leading order higher derivative operator $\nabla^2 \delta$, evaluated in Eulerian space for numerical efficiency.

EFT likelihood

By construction, our model does not capture modes above the cutoff Λ in the initial conditions. These modes introduce scatter around the mean relation $\delta_{g,\text{det}}$, which is described by the stochastic contribution expressed as the field ϵ in Eq. (2.1). The purpose of the field-level EFT likelihood is to absorb this stochastic contribution. Considering that ϵ originates from integrating out numerous independent k modes, the central limit theorem ensures that this field is Gaussian at leading order. Furthermore, owing to the local nature of tracer formation, the power spectrum of ϵ is constant at leading order, with corrections scaling as k^2 . These properties lead to the formulation of the EFT likelihood

$$\ln \mathcal{L}_{\text{EFT}}(\delta_g | \hat{s}, \theta, \{b_O\}, \sigma) = -\frac{1}{2} \sum_{k < \Lambda} \left[\ln[2\pi\sigma^2(k)] + \frac{1}{\sigma^2(k)} |\delta_g(\mathbf{k}) - \delta_{g,\text{det}}[\hat{s}, \theta, \{b_O\}](\mathbf{k})|^2 \right]. \quad (2.17)$$

where σ^2 represents the noise power spectrum, formulated in a way which ensures its positive definiteness,

$$\sigma^2(k) = \sigma_\epsilon^2(k)(1 + k^2\sigma_{\epsilon,2})^2. \quad (2.18)$$

The parameter σ_ϵ is the variance of the noise field ϵ on the discrete grid. This quantity is dependent on both the grid size, N_g^Λ , and the box size L . Its relationship with the noise power spectrum P_ϵ is then given by

$$P_\epsilon = \sigma_\epsilon^2 \frac{L^3}{(N_g^\Lambda)^3}. \quad (2.19)$$

The main feature to highlight in the EFT likelihood is that it compares the data δ_g and the model $\delta_{g,\text{det}}$ mode by mode, or voxel by voxel, up to the maximum scale at which we trust the model. This allows the likelihood to access the full spectrum of information within the field.

3 Code Implementation

In this section we briefly summarize the way the theory is implemented in the `LEFTfield` code. We start from the sampling of initial conditions. We place those on a grid of size N_g^Λ , and multiply them with the square root of the linear power spectrum to obtain the initial field. The size of the initial grid, N_g^Λ , is determined by the requirement to represent all Fourier modes (for the given box size L) up to the cutoff Λ . Next, we find the bias operators. This procedure slightly varies between the Eulerian and Lagrangian case.

In the Eulerian case, we construct the LPT displacement to second order (2LPT). During the construction, to make sure all physical modes are accounted for, we employ a grid of size $N_g^{n\Lambda}$, where $n = 2$ is the maximum perturbative order. We then displace a uniform grid of pseudoparticles to Eulerian space. These pseudoparticles are then assigned (see below) to obtain the Eulerian density field δ . This field is subsequently sharp- k filtered as described above, after which the Eulerian bias operators are constructed. We resize the grid appropriately to ensure that all modes entering the likelihood are safe from aliasing.

In the Lagrangian bias case, the set of operators listed in Eq. (2.16) is constructed concurrently with the 2LPT displacement. In addition to the uniform-weight grid used to obtain the Eulerian matter density, we also assign particles with weights given by the $O_L(\mathbf{q})$, effectively displacing the Lagrangian operators to Eulerian space [22].

The assignment schemes implemented in `LEFTfield` are nearest-grid-point (NGP), cloud-in-cell (CIC), triangular-shaped cloud (TSC) and non-uniform-to-uniform discrete Fourier transform (NUFFT) [41], which we employ as an assignment scheme. For the forward model in this paper, we use the NUFFT, as it converges rapidly with Eulerian grid size thanks to the kernel deconvolution. NUFFT implements the non-uniform-to-uniform discrete Fourier transform [$f(\mathbf{x}) \rightarrow \tilde{f}(\mathbf{k})$] by assigning particle positions \mathbf{x}_i with weights $f(\mathbf{x}_i)$ to a supersampled grid (increasing the resolution by a factor typically in the range 1.2 to 2) using a suitable assignment kernel with compact support (of roughly 4 to 16 grid cells). It then performs an FFT on the supersampled grid, deconvolves the assignment kernel, and finally performs a grid reduction in Fourier space to yield the desired uniform discrete Fourier transform $\tilde{f}(\mathbf{k})$. This method is approximate, but accuracy close to machine precision can be obtained for very reasonable computational effort. For the Eulerian grid size, we choose N_g^{Eul} such that the Nyquist frequency corresponds to $(3/2)\Lambda$, at which point the density assignment is converged to next-to-leading order [42].

Mock	Bias basis	$P_\epsilon [h^{-3} \text{Mpc}^3]$	β	b_δ	$b_{\nabla^2\delta}$	$b_{\sigma\sigma}$	$b_{\text{Tr}[M^{(1)}M^{(1)}]}$	b_{δ^2}	b_{K^2}
A	Lagrangian	553.83	0.99	1.21	0	-0.26	-0.18	-	-
B	Eulerian	915.53	0.98	1.67	-0.07	-	-	-0.19	0

Table 1: Values of parameters used to produce mock datasets A and B. For both mocks, we use second order LPT combined with second order bias expansion and cutoff $\Lambda_0 = 0.3 h \text{Mpc}^{-1}$.

4 Synthetic Data sets

The data sets used in this paper were generated using the `LEFTfield` code, which we denote as Mock A and Mock B. Both data sets were generated in a box of side length $L = 2000 h^{-1} \text{Mpc}$ and with fiducial cosmology fixed to $\sigma_8 = 0.85$, $\Omega_m = 0.3$, $\Omega_\Lambda = 0.7$, $h = 0.7$ and $n_s = 0.967$. We emphasize that both mocks contain nonlinear information, as they were generated using second-order LPT, while the distinguishing factor between them lies in the choice of the bias model. Mock A was created using the second-order Lagrangian bias, while Mock B utilized the second-order Eulerian bias. For the bias parameters, we adopted values obtained through fixed-phase inference on realizations of halo catalogues (see for example [43]), specifically the halo mass range $\log_{10}(M/h^{-1}M_\odot) = 13.0 - 13.5$ at redshift $z = 0$. In order to increase the signal to noise ratio, we used a slightly lower noise level than in the halos sample for both mocks. Ground truth β_0 values were deliberately selected to be different from 1 to verify unbiased inference even in the case of a nontrivial rescaling of the fiducial power spectrum. Furthermore, the mocks were generated at the cutoff $\Lambda_0 = 0.3 h \text{Mpc}^{-1}$, while the inference was performed at lower Λ values, allowing us to test the impact of model mismatch in this dimension as well. The values of all parameters used to generate these mocks are summarized in Table 1.

5 Field level BAO inference

5.1 Sampling method and data analysis

In this section, we provide a detailed account of how we sample from the posterior defined in Section 2. To achieve this, we employ a combination of the Hamiltonian Monte Carlo (HMC) sampler for initial conditions and the slice sampler for all other parameters.

The initial step involves selecting a prior for the initial field \hat{s} . Depending on this choice, we distinguish between two scenarios,

$$\hat{s}(\mathbf{x}) = \begin{cases} \delta_D(\hat{s} - \hat{s}_{\text{true}}), & \text{FixedIC,} \\ \mathcal{N}(0, 1), & \text{FreeIC.} \end{cases} \quad (5.1)$$

In the case when \hat{s} is fixed to ground truth, we are talking about FixedIC case. Alternatively, the case when the Gaussian prior for \hat{s} is chosen, we denote as FreeIC. FixedIC case has been extensively studied in our previous work [16], while here we are focused on the FreeIC case and use the FixedIC case only as a consistency check.

The FreeIC case is challenging in particular due to the dimensionality of the parameter space of \hat{s} which is of the order of 10^6 . To perform the sampling of such a large parameter space, we use the HMC sampler which is well suited for sampling in large dimensions. While

the execution time in standard MCMC techniques typically scales linearly with the dimension of the problem N_{dim} , in the case of the HMC it scales as $N_{\text{dim}}^{1/4}$ [27]. Because of the way HMC generates new proposals, it requires a forward model which is differentiable with respect to the initial conditions. Fortunately, our forward model is differentiable, and the structure of the `LEFTfield` code allows us to find its analytical derivative by performing successive applications of the chain rule.

Apart from the initial conditions, we also sample β, σ_ϵ and $\sigma_{\epsilon,2}$. The priors used for these parameters are

$$\begin{aligned}\mathcal{P}(\beta) &= \mathcal{U}(0.8, 1.2), \\ \mathcal{P}(\sigma_\epsilon) &= \mathcal{U}(0.05, 100), \\ \mathcal{P}(\sigma_{\epsilon,2}) &= \mathcal{U}(-10^5, 10^5),\end{aligned}\tag{5.2}$$

where \mathcal{U} denotes the uniform distribution.

When employing the likelihood marginalized over bias parameters, one MCMC chain used Gaussian priors for bias parameters. More specifically, the priors used were $\mathcal{N}(0.01, 5)$ for b_δ and $\mathcal{N}(0, 5)$ for the other bias parameters. In addition to this, we operated two other chains that employed uniform priors: $\mathcal{U}(0.01, 10)$ for b_δ , and $\mathcal{U}(-30, 30)$ for the remaining bias parameters. However, the bias coefficients are well constrained by the data, and the posteriors are likelihood-dominated for both chains. Hence, despite the different priors, all chains are found to yield consistent posteriors in β, σ_ϵ and $\sigma_{\epsilon,2}$. Therefore, we aggregated the results from all three chains in the analysis. For comparison, we have also performed inferences using a likelihood that was not marginalized over bias parameters; the results of this inference are shown in App. A, and provide evidence for the above statement.

To sample cosmological parameters, we employ the univariate slice sampling technique. This involves drawing samples from the one-dimensional probability density function associated with these parameters, considering the present state of the initial conditions, \hat{s} . For each data set, we run a set of three chains: one starting from true initial conditions and two starting from random initial conditions. We continue running these chains until we achieve at least 100 effective samples of the β parameter.

5.2 Field-level results

In this section, we present inference results obtained using the marginalized EFT likelihood for both Mock A and Mock B.

Mock A was generated using Lagrangian bias expansion which we also use for the inference. In Fig. 1, we present a trace plot for the parameter β corresponding to a specific value of $\Lambda = 0.2 h \text{ Mpc}^{-1}$. The figure shows the trajectories of all three Markov chains utilized in our analysis. Despite starting from different β values, the chains exhibit rapid convergence towards a consistent value of β , indicating robustness in parameter estimation across varied starting points. It is also important to note that one of the chains started from the true initial conditions \hat{s}_{true} while the other two started from random \hat{s} . Fig. 2 depicts the normalized auto-correlation function for β (for $\Lambda = 0.2 h \text{ Mpc}^{-1}$), for one of the chains. We find the correlation length $\tau(\beta)$ to be quite short, substantially shorter than that of σ_8 in the field-level inference chains shown in [24, 44]. This is a major computational advantage which also allows us to push to smaller scales than used there. We determine the effective number of samples by dividing the absolute length of the chain by the estimated correlation length.

Our main findings for Mock A are summarized in Fig. 3. In the left panel, we show the remaining systematic bias in the β value. For the lower cutoffs, $\Lambda = 0.15 h \text{ Mpc}^{-1}$ and $\Lambda =$

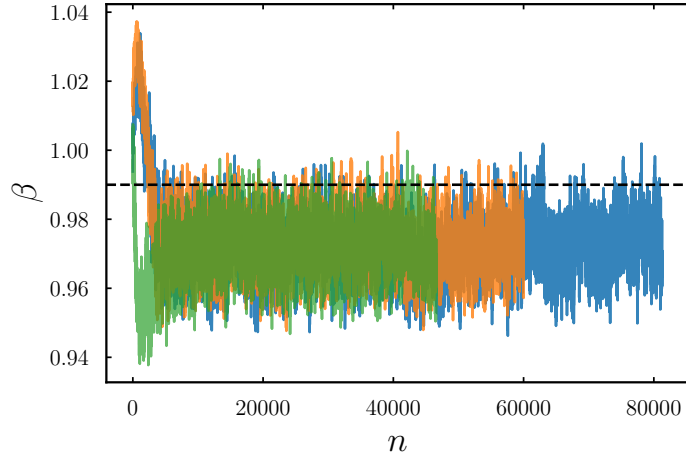


Figure 1: Trace plot of parameter β for $\Lambda = 0.2 h \text{Mpc}^{-1}$ for three independent MCMC chains, where n denotes the sample index. The chain shown in green started from the true initial conditions \hat{s}_{true} while the other two chains started from random initial conditions \hat{s} . Each chain started from a different initial β value, with all quickly converging to the same value. Dashed black line indicates the ground truth value β_0 .

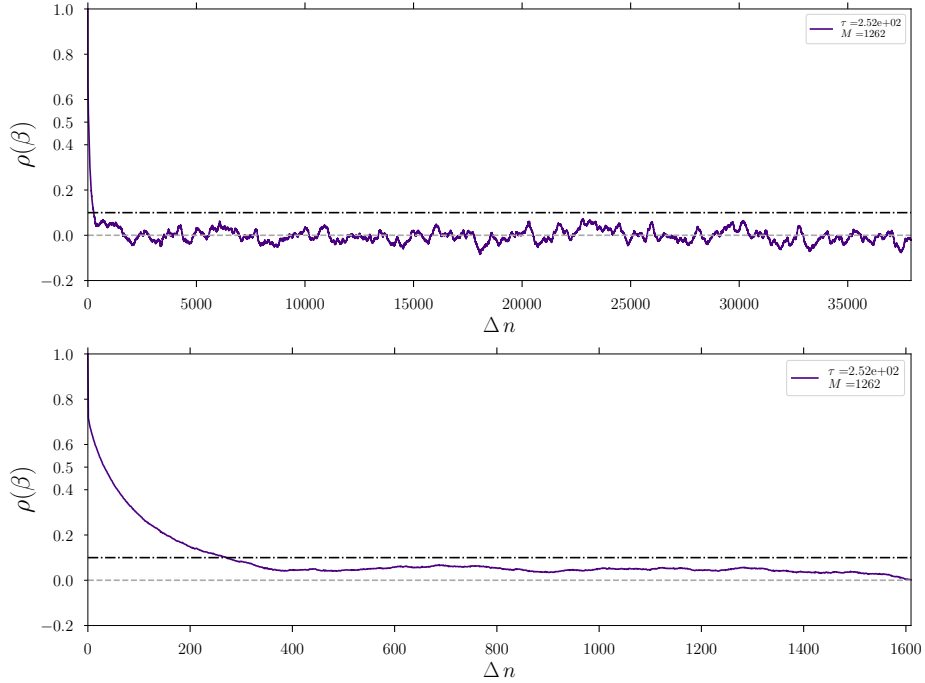


Figure 2: The normalized auto-correlation function for parameter β inferred at $\Lambda = 0.2 h \text{Mpc}^{-1}$. In the figure we also display the correlation length value τ together with the maximum separation M between the samples considered, both of which are defined in App. A. The correlation length of β is estimated to be $\tau \simeq 244$ samples. In the lower panel, we zoom into the first 1800 samples of the chain.

$0.18 h \text{ Mpc}^{-1}$, the bias is below 1%, however in the case of $\Lambda = 0.2 h \text{ Mpc}^{-1}$ the systematic offset is around 1.8%. This is most likely due to our choice to employ a second-order bias expansion for the inference. We generated the mocks at a higher cutoff, and thus they require more bias terms to describe at the lower cutoff used for the inference.

The right panel of Fig. 3 displays the 68% confidence-level error bars for β , denoted as $\sigma_{\text{F}}(\beta)$, obtained through the EFT likelihood across varying Λ values. For the lowest cutoff, $\sigma_{\text{F}}(\beta)$ slightly exceeds 1%, whereas for the two higher cutoffs, it reduces to 0.71% and 0.66%, respectively. The reduction in error bar size with increasing cutoff was anticipated, as a larger Λ permits the inclusion of more modes in both the forward model and the likelihood, thereby providing additional information. We can also compare the behavior of $\sigma_{\text{F}}(\beta)$ as a function of Λ with the ideal expectation from mode counting, $\sigma_{\text{F}}(\beta) \propto N_{\text{mode}}^{-1/2}(\Lambda)$, finding very rough agreement. More precisely, the error bar $\sigma_{\text{F}}(\beta)$ improves more rapidly than the mode scaling between $\Lambda = 0.15 h \text{ Mpc}^{-1}$ and $\Lambda = 0.18 h \text{ Mpc}^{-1}$, while between $\Lambda = 0.18 h \text{ Mpc}^{-1}$ and $\Lambda = 0.2 h \text{ Mpc}^{-1}$, it shrinks at a lower rate than estimated from mode counting. Note however that the simple mode counting ignores the varying sensitivity to a change in β of the linear power spectrum as a function of k .

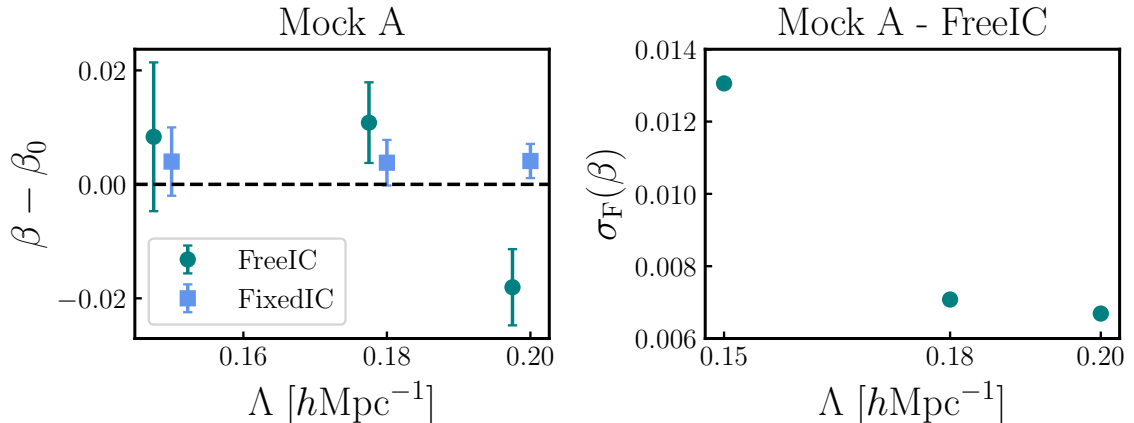


Figure 3: Inference results for the Mock A. Left panel shows inferred BAO scale relative to ground truth obtained using Lagrangian bias for sampling. FreeIC are represented using circle marker and FixedIC using a square. On the right we show the 68% CL error bar on the BAO scale, $\sigma_{\text{F}}(\beta)$, as a function of cutoff Λ .

Turning our attention to Mock B, this data set is generated using Eulerian bias and sampled with both Eulerian and Lagrangian bias. The left panel of Fig. 4 shows the inferred β for both Eulerian and Lagrangian bias cases. In the instance of Eulerian bias, we observe that the residual systematic bias remains below 1% across all considered cutoffs. Additionally, the ground truth value of β is consistently recovered within 1σ . Conversely, when using the Lagrangian bias model for inference, a slightly higher systematic bias is evident. Specifically, for $\Lambda = 0.15 h \text{ Mpc}^{-1}$ and $0.18 h \text{ Mpc}^{-1}$, this bias hovers around 1%, while for $\Lambda = 0.2 h \text{ Mpc}^{-1}$, it increases somewhat to 1.7%. This is consistent with what we found for Mock A, and would likely be solved by going to a higher order in bias in the inference.

In the right panel of Fig. 4, we show the inferred 68% CL error bar $\sigma_{\text{F}}(\beta)$ for the Mock B at the different cutoffs. We find that in the case of both bias models the size of the error

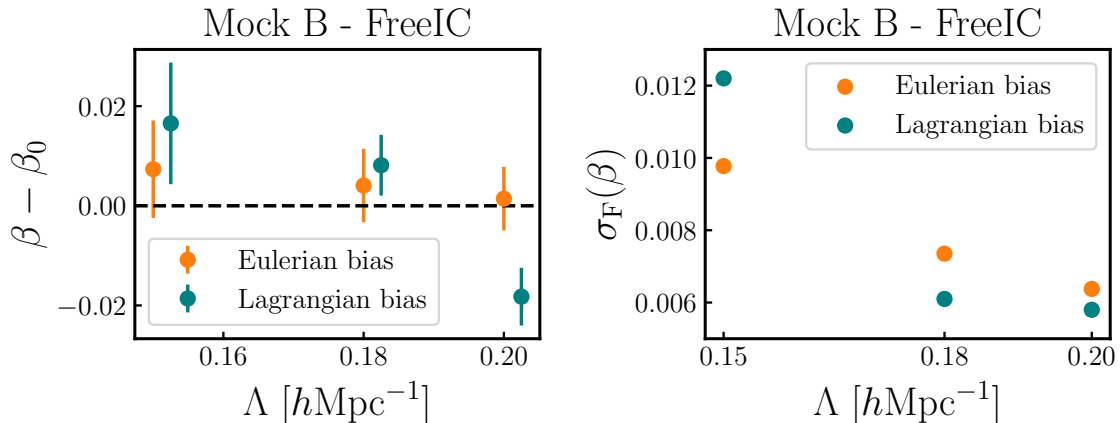


Figure 4: Inference results for Mock B. The left panel displays the inferred BAO scale relative to the ground truth, where the BAO scale is sampled alongside the initial conditions. The Lagrangian bias points, computed for the same values of Λ , have been slightly displaced horizontally for better visibility. On the right, we show the 68% CL error bar, $\sigma_F(\beta)$, as a function of the cutoff Λ . The results obtained using the Lagrangian bias are depicted in blue, while those obtained using Eulerian bias are shown in orange.

bar is shrinking with increasing Λ . This trend aligns with our expectations, as a larger Λ implies the inclusion of more modes in both the forward model and the likelihood.

Comparing the error bar size, $\sigma_F(\beta)$, between the Eulerian and Lagrangian models shows that the error bar is smaller in the case of the Lagrangian bias model. This difference is likely attributable to the construction of bias operators in these models. In the Eulerian bias model, bias operators are constructed using the filtered matter field, δ_Λ . This second filter (in addition to the one applied to the initial conditions) removes some mode-coupling contributions that are under control and kept in the Lagrangian bias model, which only filters the initial conditions (both bias models of course use the same likelihood filter). The downside of the Lagrangian approach is the higher computational cost due to the additional density assignments needed.

In Fig. 5, we show posteriors of parameters sampled on the Mock B dataset using $\Lambda = 0.18 h \text{Mpc}^{-1}$. The two panels correspond to the Eulerian and Lagrangian biases, respectively. Mock B was generated at $\Lambda_0 = 0.3 h \text{Mpc}^{-1}$ with $\sigma_\epsilon = 0.9$. From Eq. (2.19), we find that this will correspond $\sigma_\epsilon \approx 0.41$ at $\Lambda = 0.18 h \text{Mpc}^{-1}$. We see that the inferred value of σ_ϵ is indeed consistent with the expected value within errors. However, we notice that $\sigma_{\epsilon,2}$ is now larger than zero. This elevation in noise level is due to the fact that inference is performed at $\Lambda < \Lambda_0$. Since the model is nonlinear, the modes between Λ and Λ_0 which are integrated out lead to additional effective noise contributions, as shown explicitly in [23] and at the level of renormalization-group equations in [45].

6 Comparing the field-level results to the reconstruction approach

6.1 BAO Reconstruction Procedure

We now describe how we implement a BAO reconstruction pipeline on our mock data. The initial step involves generating mock datasets using the `LEFTfield` code. The parameters

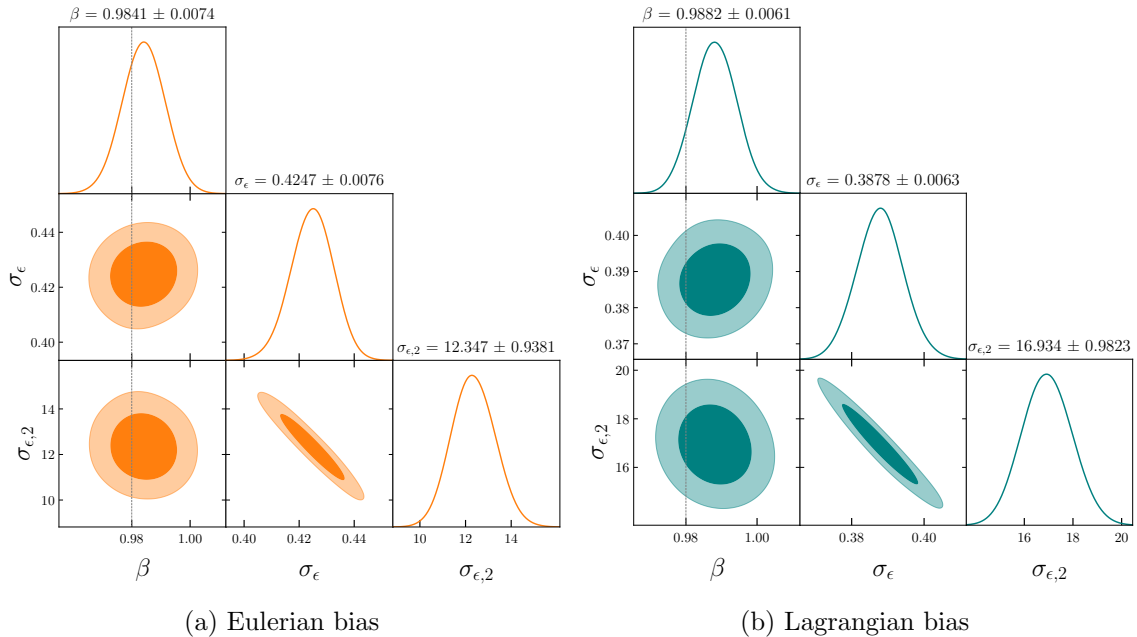


Figure 5: Posterior of parameters for the FreeIC inference in the case of Mock B. Left panel (a) represents the Eulerian bias model while the right panel (b) represents the Lagrangian bias. The dotted gray line indicates the ground truth value β_0 in each case. The inference was performed at $\Lambda = 0.18 h \text{Mpc}^{-1}$ in both cases.

chosen for the creation of these datasets are aligned with those employed in the field-level inference (as described below) to maintain consistency across the two analyses. This includes the use of the same bias parameters, noise levels, and the value for β . A flowchart summarizing both analyses is shown in Fig. 6.

We adopt the standard reconstruction procedure, which is based on the algorithm introduced by [5]. However, before this can be applied, we need to convert the density distribution on a grid (of size $N^{\Lambda_0} = 192^3$, where $\Lambda_0 = 0.3 h \text{Mpc}^{-1}$ is the cutoff value used to generate the mock) generated by the `LEFTfield` code to a catalog of discrete “tracer” positions. This is done by first replacing the Gaussian likelihood used in the EFT likelihood with a Poisson process, which generates a discrete tracer count N_i in each voxel i . For the average tracer number density \bar{n}_g , we adopt the value of $1/P_\epsilon$ used for the mocks employed in the field-level analysis. We then assign random positions to each of the N_i tracers within the voxel i .

Once the mock catalog is obtained, we proceed with the reconstruction. To ensure a fair comparison with the field level approach and guarantee that both methods have access to the same k -modes, we carefully select the smoothing scale and grid sizes. The choice of the smoothing scale is particularly important, given that the field-level approach employs a sharp- k filter, while standard reconstruction involves a Gaussian filter. We choose the Gaussian smoothing scale $R = \frac{1}{\Lambda}$. We consider this to be a conservative choice for the comparison, as it allows for a significant contribution from modes with $k > \Lambda$ in the standard reconstruction approach, while these modes are excluded from the field-level analysis.

The reconstruction proceeds as follows.

1. Smooth the density field δ_g using a Gaussian filter $S(k, R)$ with a smoothing scale R : $\delta_g(\mathbf{k}) \rightarrow S(k, R)\delta_g(\mathbf{k})$.

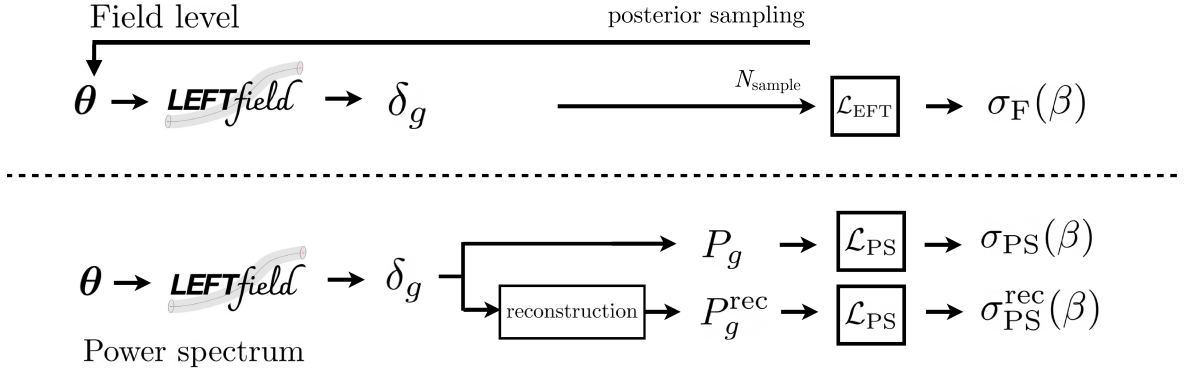


Figure 6: Diagram of two methods of BAO inference; field level inference (top) and power spectrum-based inference with and without reconstruction (bottom). The reconstruction step includes the generation of a discrete tracer catalog from δ_g , as described in the text

- Using the smoothed density field, we find the estimated displacement ψ , where

$$\psi(\mathbf{k}) \equiv -i \frac{\mathbf{k}}{k^2} S(k, R) \frac{\delta_g(\mathbf{k})}{b_\delta}. \quad (6.1)$$

- We interpolate ψ to find its value at the position of each tracer and use it to move the tracers.
- Once all the tracers have been shifted, we use the nearest-grid-point (NGP) assignment scheme and a grid of size N^{Λ_0} to obtain the “displaced” density field δ_d . Notice that this operation removes a large fraction of the large-scale perturbations in δ_g .
- We generate a spatially uniform grid of particles and shift them by ψ to create the “shifted” field δ_s . The assignment scheme used to find δ_s is again NGP, and the grid size is N^{Λ_0} . Notice that this operation removes a large fraction of the large-scale perturbations in δ_g .
- The reconstructed density field is obtained as $\delta_g^{\text{rec}} = \delta_d - \delta_s$, where the field $-\delta_s$ reinstates the large-scale perturbations removed from δ_d .
- Next, we resize the reconstructed field to a grid of size N_g^Λ to make sure we keep only the modes below the cutoff.
- Finally, we measure the power spectrum of the reconstructed field, P_g^{rec} , with $k_{\text{max}} = \Lambda$.

As an illustration, the left panel of Fig. 7 displays the oscillatory part of the power spectrum averaged over 500 Mock A-like realizations, for both pre- and post-reconstruction cases. Post-reconstruction, the wiggles become significantly more pronounced.

Finally, to obtain the BAO scale parameter β and its uncertainty, we use a maximum-likelihood approach, where all parameters apart from β are fixed to their ground truths. For a given value of Λ , we calculate the power spectrum likelihood \mathcal{L}_{PS} for a set of $\{\beta_i\}$ values, where

$$-2 \log \mathcal{L}_{\text{PS}}(\beta) = \frac{(P_{\text{data}}(k) - P_{\text{theory}}(k, \beta))^2}{\text{Cov}[P_{\text{data}}(k)]} + \text{const.} \quad (6.2)$$

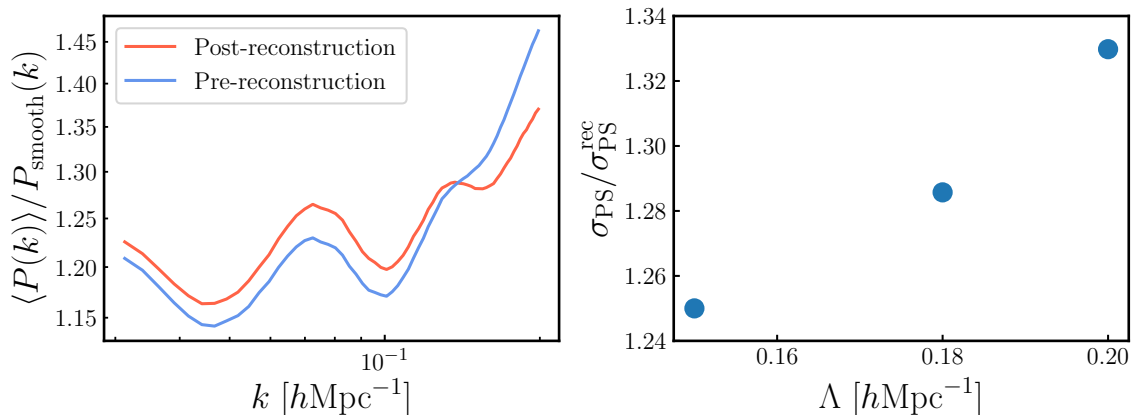


Figure 7: The left panel shows the oscillatory part of the power spectrum averaged over 500 Mock A-like realizations. We show this for both the pre- and post-reconstructed power spectrum (for $\Lambda = 0.2 h\text{Mpc}^{-1}$). We see that following the reconstruction, the wiggles on smaller scales become more pronounced. The right panel shows the inferred error bar $\sigma_{\text{PS}}(\beta)$ on the BAO scale using pre- and post-reconstruction power spectrum. The gain in BAO scale precision due to reconstruction increases as Λ increases.

Here, $P_{\text{data}}(k)$ represents the power spectrum of the reconstructed mock data from which we aim to infer the BAO scale, and $P_{\text{theory}}(k, \beta)$ is the theoretical prediction for the reconstructed power spectrum for different β values. We find the latter by averaging over 500 samples, each sharing the same cosmological, bias, and noise parameters at fixed β , but featuring independent realizations of the initial conditions. We use linear binning to find the power spectrum. The forward model, specified by Λ_0 , as well as all bias terms and σ_ϵ are fixed at the values used for generating the mock. It is worth noting that $P_{\text{theory}}(k, \beta)$ already incorporates the stochastic contributions P_ϵ . We use the linear covariance

$$\text{Cov}[P_{\text{data}}(k)] = 2 \frac{[P_{\text{theory}}(k, \beta_0)]^2}{m_k}, \quad (6.3)$$

where m_k is the number of modes inside a bin. Since the covariance is independent of β , the normalization constant in Eq. (6.2) is irrelevant.

We then fit a parabola to the set of $\{\beta_i, -2 \ln \mathcal{L}_{\text{PS}}(\beta_i)\}$. The maximum-likelihood value of β , denoted as $\hat{\beta}$, is located at the minimum of this parabola. The error bar, $\sigma_{\text{PS}}(\beta)$, can be estimated by finding the point at which $-2 \log \mathcal{L}_{\text{PS}}$ increases by 1. Note that we apply this inference procedure using \mathcal{L}_{PS} both for the pre- and post-reconstruction power-spectra, as depicted in Fig. 6. The improvement in BAO scale determination after reconstruction is demonstrated in the right panel Fig. 7. Notice that the relative improvement grows with increasing Λ , which is expected since the sharpening of the BAO by reconstruction is more pronounced at higher k .

Compared to the field-level approach, which jointly infers all bias and stochastic parameters, this analysis strongly favors the standard power-spectrum-based method. By conducting the reconstruction at the same cutoff used to generate the mock, we give access to the complete information about the mock, and avoid the model mismatches that the field-level analysis had to overcome. Additionally, we fix the values of the bias parameters, whereas in

practice, jointly inferring the values of the bias parameters would introduce further uncertainties into the inference process and enlarge the error bars. These issues are clearly worth revisiting in the future.

6.2 Inference results and comparison with the field level

In this section, we compare the results of the power spectrum analysis (before and after reconstruction) with the field-level inference presented in the previous section.

We begin with Mock A, presenting in Fig. 8 the ratio of error bars on $\hat{\beta}$ derived from the two power-spectrum-based analyses, σ_{PS} , to those obtained at the field level, σ_{F} . Compared to the field level, the pre-reconstruction power spectrum yields an error bar between 1.15 and 2 times larger. As expected, this difference between σ_{PS} and σ_{F} decreases once we perform reconstruction, where we find σ_{PS} to be at most 1.5 times larger than σ_{F} . Note that the improvement of field level over power spectrum generally increases with the cutoff. There are several possible explanations for this, which we turn to in the discussion Sec. 7.

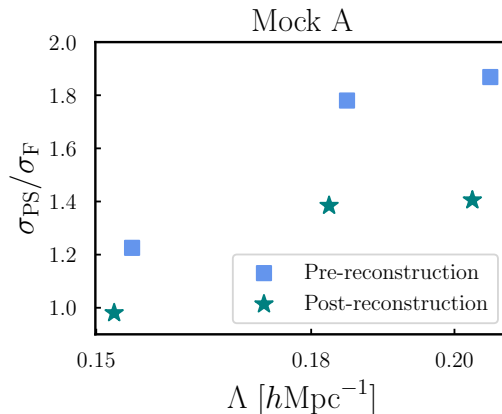


Figure 8: Inferred error bar $\sigma_{\text{PS}}(\beta)$ on the BAO scale using pre- and post-reconstruction power spectrum, relative to that in the field-level inference σ_{F} , in the case of Mock A. This mock was generated (and sampled, in case of field-level inference) using Lagrangian bias. Pre-reconstruction results are depicted using squares, whereas post-reconstruction results are represented by stars. It is evident that, even comparing to power spectrum after BAO reconstruction, the field-level BAO scale inference is more precise, by up to a factor of 1.4, corresponding to a ~ 2 times larger survey volume.

We perform a similar analysis in the case of the Mock B, the results of which are summarized in Fig. 9. In the plot, the orange points represent the comparison of the post-reconstruction power spectrum variance σ_{PS} to the case when we use Eulerian bias expansion in the field level. Blue points correspond to Lagrangian bias expansion being used for the field level. We find that results here are consistent with the ones in the case of Mock A: σ_{PS} (after reconstruction) is between 1.1 and 1.6 times larger than σ_{F} , with the improvement generally increasing toward higher Λ .

7 Discussion and Conclusions

In this paper, we have presented the outcome of field-level BAO scale inferences, which jointly infer the BAO scale together with the initial conditions, bias and stochastic parameters via the

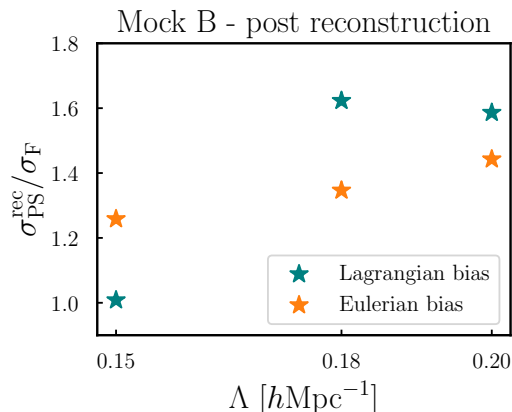


Figure 9: Inferred error bar $\sigma_{\text{PS}}(\beta)$ on the BAO scale from the post-reconstruction power spectrum, relative to that in the field-level inference σ_{F} , in the case of Mock B. Blue points indicate the scenario where the Lagrangian bias is used in the field level inference, while orange points correspond to the Eulerian case (the reconstruction results are the same in both cases). The field-level error bar is consistently smaller, regardless of which bias basis is used in the field-level inference.

LEFTfield code, applied to mock data in the rest frame (without redshift-space distortions). The mock datasets were created using bias parameters taken from a fixed initial condition (FixedIC) analysis on halo catalogues, and at a substantially higher cutoff (or resolution) than those used in the inference. By introducing model misspecification in this way, we attempt to make our mocks as realistic as possible. The primary distinction between the two sets of mock data is in the bias expansion model employed for their generation: Mock A was produced using the second-order Lagrangian bias, whereas Mock B used the second-order Eulerian bias.

For Mock A, the analysis was done only using the second-order Lagrangian bias expansion in the inference. It showed that the systematic bias in β stays below 1% and is effectively negligible for all Λ values, except for the highest cutoff, where it increases to about 1.8%. We plan to investigate this increase in systematic bias in β in the future by going to the third order in the bias expansion.

For the Eulerian-bias Mock B, our analysis included both second-order Lagrangian and Eulerian biases. For the Eulerian bias, we find that the remaining systematic bias is consistent with zero and decreases as Λ increases. In the case of Lagrangian bias expansion, the remaining systematic bias is slightly higher. Again, it is possible that the residual systematic shift in the Lagrangian analysis decreases once we go to a higher order in bias expansion. Furthermore, we find that the error bar in the case of the Lagrangian analysis is lower than in the case of Eulerian analysis. This is likely connected to the approaches used for constructing bias operators in these models. For the Eulerian bias model, the construction of bias operators involves an additional filtering of the matter field, beyond the initial condition filtering. This extra filtering step results in the omission of some mode-coupling contributions, which are preserved in the Lagrangian bias model. The latter only applies filtering to the initial conditions. Note that both models utilize the same likelihood filter.

The standard approach to BAO inference is based on applying a reconstruction procedure to the tracer catalog, and then measuring the BAO scale in the post-reconstruction

power spectrum. In Sec. 6, we detailed the application of this reconstruction algorithm to our mock data. Throughout the reconstruction process, we employed the same Λ_0 , and fixed the bias parameters to the values that were used to generate the mock datasets, thereby giving a significant benefit to the reconstruction-based analysis pipeline. Figures 8 and 9 summarize the comparison between the error bars obtained from the field level analysis, σ_F , and those derived using the power spectrum, σ_{PS} . These figures illustrate that, depending on the mock and the value of Λ , σ_F is smaller than σ_{PS} by up to a factor of two (pre-reconstruction), or between 1.4 and 1.6 (post-reconstruction), the latter corresponding to an effective doubling of the survey volume. Additionally, we observe that the improvement over the power spectrum analysis increases as more modes are included with increasing Λ .

These results are clearly very encouraging for the field-level approach. However, one might naturally ask two questions about these findings: first, where does the additional information come from? As argued in [15], the field-level approach extracts the BAO feature not only in the power spectrum, but also in higher n -point functions of the tracer, such as the bispectrum, as it does not rely on any compression of the data. In addition, our use of a 2LPT forward model means that the change of the local BAO scale in the presence of large-scale density perturbations (due to the different local expansion in the separate-universe picture) is consistently captured. On the other hand, the Zeldovich approximation used in Eq. (6.1) does not describe this effect correctly [4]. Both of these effects are expected to become more significant as smaller scales are included in the analysis, which could explain the increasing improvement that we find toward smaller scales (higher Λ).

It is worth noting that the maximum wavenumbers included in our analysis are somewhat lower than those chosen in current BAO reconstruction analyses. Specifically, these choose a smoothing kernel in the displacement construction on similar scales as the one used here, but then measure the post-reconstruction power spectrum to higher $k \sim 0.3 - 0.5 h \text{ Mpc}^{-1}$. This approach assumes that the BAO are still well described by the perturbative model on scales where perturbation theory no longer applies, an assumption which needs to be carefully validated. On the other hand, the field-level approach by construction requires that the model describe all aspects of the data up to the maximum scale included, which precludes us from pushing this approach beyond perturbative scales.

The second natural question is whether these results apply to actual nonlinear tracers. Thus, our next step will be to transition from mock data to dark matter halos in full N-body simulations, and perform a similar comparison there. We are also advancing our redshift-space modeling [25], which will enable an anisotropic BAO scale inference in terms of line-of-sight and perpendicular components. Moreover, we plan to jointly infer the BAO scale while varying cosmological parameters governing the growth, such as σ_8 and the growth rate f .

Finally, the field-level forward model also enables a consistent Bayesian inference of the BAO scale using the BAO reconstruction technique, by way of simulation-based inference (SBI) [46], allowing us to consistently marginalize over bias, noise and cosmological parameters. We also plan to explore this direction in the near future.

Acknowledgments

We would like to thank Andrija Kostić for useful discussions and help with the MCMC analysis. We would also like to thank Julien Lesgourgues, Şafak Çelik, Minh Nguyen, Ivana Nikolac and Julia Stadler for many helpful discussions.

A Data Analysis

A.1 Correlation length

In this section, we describe in detail how we conducted the analysis of field-level chains. We follow the same procedure for both mocks. For each bias expansion used to perform the inference, we analyze three Λ values. For each Λ , we run three chains. For one chain, we leverage our knowledge of the ground truth for the initial conditions and start sampling from there. The other two chains begin from random initial conditions, with a different seed used for each to ensure they start from a unique set of initial conditions. All three chains also had slightly different initial values for the cosmological parameters sampled. This approach ensured that the inferred value of BAO is independent of the sampler’s starting point. As mentioned in the Sec. 5.1, one chain used Gaussian prior for bias, while the other two used uniform priors; however, these priors were essentially uninformative, as the bias parameters are well constrained by the data (at least when sampling only β as cosmological parameter),

To perform the analysis, we combine the three independent chains into one large chain, which consists of N elements; for a parameter f , we label the sample points as $\{f_s\}$, after discarding the burn-in portion of each chain, which was about 5 correlation lengths. To denote the mean of the dataset, we use $\langle f_s \rangle \equiv \bar{f} = \frac{1}{N} \sum_{s=1}^N f_s$. We continue running the chains until we achieve 100 effective samples of the β parameter for each dataset and Λ considered. The number of effective samples is calculated by dividing the total number of samples, N , by the auto-correlation length. The auto-correlation length for an MCMC chain indicates the number of steps required within the chain to obtain samples that are independent of each other. Correlation length can be estimated using the relation

$$\hat{\tau}_f(M) = 1 + 2 \sum_{\tau=1}^M \hat{\rho}_f(\tau), \quad (\text{A.1})$$

where $\hat{\rho}$ is the normalized autocorrelation function

$$\rho(\tau) = \frac{\mathcal{A}(\tau)}{\mathcal{A}(0)}, \quad (\text{A.2})$$

and

$$\mathcal{A}(\tau) = \langle f_s f_{s+\tau} \rangle_s - \langle f_s \rangle_s^2. \quad (\text{A.3})$$

is the auto-correlation function. M is the maximum separation between the samples considered. As the best choice for M , [47] suggests using the smallest value of M such that $M \geq C \hat{\tau}_f(M)$ for a constant C chosen to minimize the covariance of the estimator. This is usually achieved for values of C close to 5. Plots indicating τ_f values of β for chains analyzed in the paper are shown below. In the tables below, we summarize the correlation lengths for the parameter β .

A.2 Parameter posteriors: marginalized likelihood

Below we present the corner plots showing posterior distribution of parameters sampled for both mocks and cutoffs. Results for the Mock B are summarized in the Fig. 10, where again we denote Lagrangian bias results in blue and Eulerian in orange. We notice the same trend of increasing noise as we did in Sec. 5.2. In Fig. 11, we present the results for Mock A. The effective noise also grows in the case of Mock A, but in this case it is σ_ϵ that grows more significantly, rather than $\sigma_{\epsilon,2}$.

$\Lambda [h \text{ Mpc}^{-1}]$	0.15	0.18	0.2
	τ		
Chain 1	210	683	101
Chain 2	165	728	132
Chain 3	175	609	261

Table 2: Correlation length values for chains run on the Mock A using Lagrangian bias.

$\Lambda [h \text{ Mpc}^{-1}]$	0.15	0.18	0.2
	τ		
Chain 1	350	252	507
Chain 2	272	771	728
Chain 3	212	123	609

Table 3: Correlation length values for chains run on the Mock B using Lagrangian bias.

$\Lambda [h \text{ Mpc}^{-1}]$	0.15	0.18	0.2
	τ		
Chain 1	186	590	735
Chain 2	105	606	744
Chain 3	800	522	710

Table 4: Correlation length values for chains run on the Mock B using Eulerian bias.

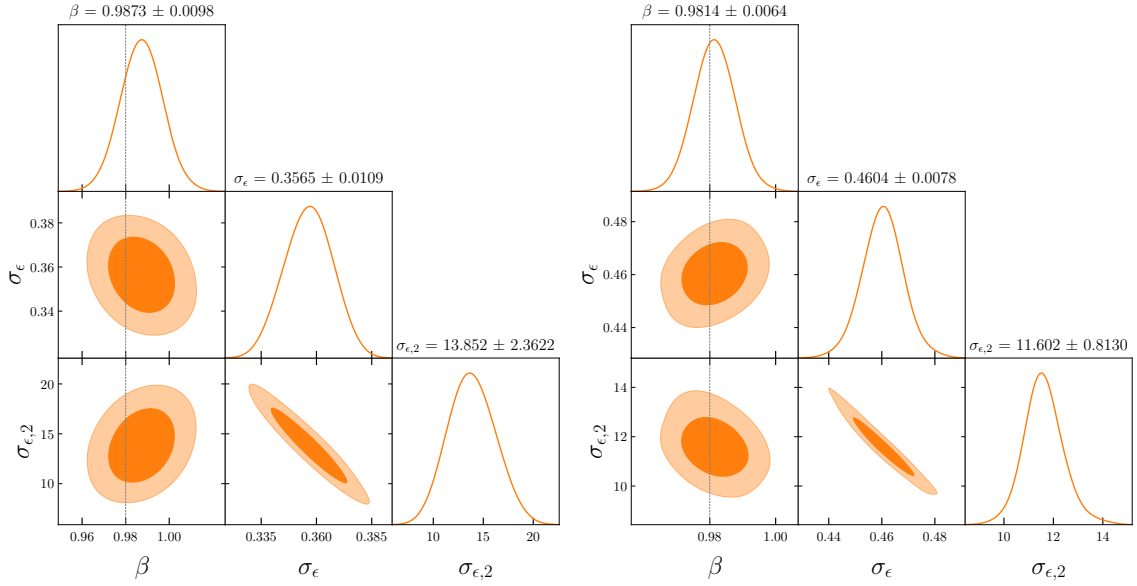
A.3 Parameter posteriors: non-marginalized likelihood

In this section, we present the results of the inference obtained using a likelihood that was not marginalized over the bias parameters. For this analysis, uniform priors were applied to the bias parameters. Specifically, a uniform prior of $\mathcal{U}(0.01, 10)$ was used for b_δ , while all other bias parameters were assigned a uniform prior of $\mathcal{U}(-30, 30)$. For the inference process, two chains per sample were initiated, each starting from random initial conditions \hat{s} and a different initial value of β . These chains converged quickly to a similar β value, as illustrated in Figure 12, which displays the trace plot of β for Mock B sampled with Eulerian bias at $\Lambda = 0.15 h \text{ Mpc}^{-1}$. The chains were run until 100 effective samples were obtained.

In Fig. 13 we show the auto-correlation plot for one of the chains. We see that the correlation length for β is very short even in the case when the non-marginalized likelihood is used. In fact, the correlation length is shorter than for the marginalized likelihood in this case (Tab. 4), in contrast to the findings for σ_8 in [23]. This finding is clearly worth further investigation; note that the parameter posteriors show no significant correlations of β with any other parameter.

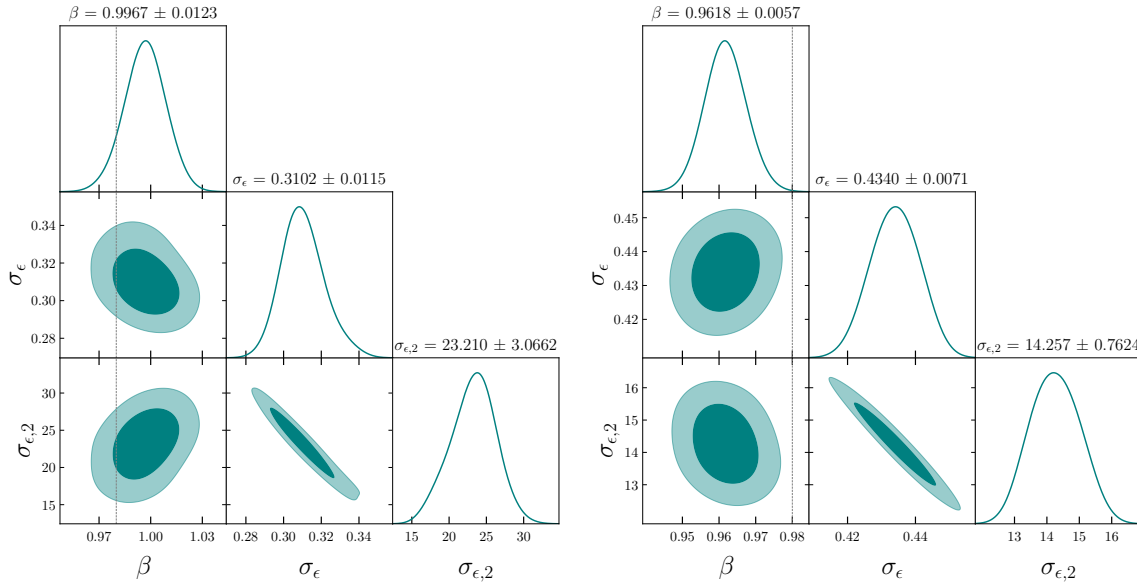
Finally, Figure 14 displays the corner plots for all sampled parameters, including the mean value and the size of the error bars for each parameter. Comparing the size of the error bars for $\sigma(\beta)$ in this plot with those in Figure 10a reveals that the error bar size for β does not depend on the type of likelihood used, as expected. Furthermore, the values of σ_ϵ and $\sigma_{\epsilon,2}$ are consistent with those obtained using the marginalized likelihood.

The inferred values of the bias parameters differ from those used to generate the mock data, due to the mismatch in Λ between the generation and sampling of the mock data [32].



(a) Eulerian bias, $\Lambda = 0.15 h \text{ Mpc}^{-1}$.

(b) Eulerian bias, $\Lambda = 0.2 h \text{ Mpc}^{-1}$.



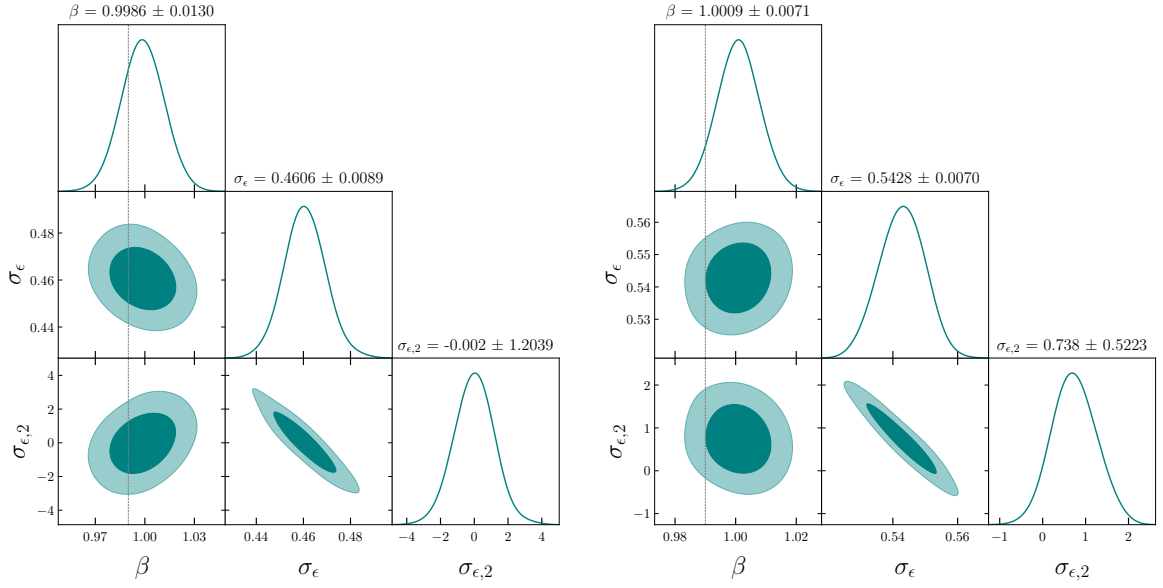
(c) Lagrangian bias, $\Lambda = 0.15 h \text{ Mpc}^{-1}$.

(d) Lagrangian bias, $\Lambda = 0.2 h \text{ Mpc}^{-1}$.

Figure 10: Posterior of parameters for the inference performed on Mock B. Top two panels (orange color) corresponds to Eulerian bias, while the lower two panels (blue) correspond to Lagrangian bias. The intermediate cutoff $\Lambda = 0.18 h \text{ Mpc}^{-1}$ behaves similarly, and is not shown here for brevity.

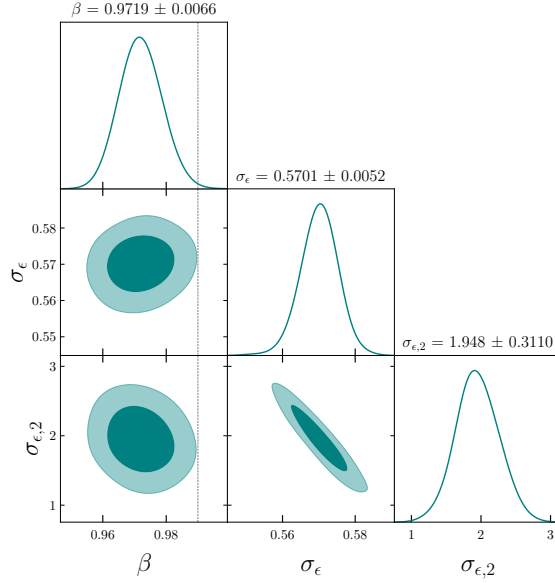
That is, the bias parameters and stochastic parameters are expected to run with Λ , while the inferred cosmological parameter, in this case β , should be consistent with the ground truth value.

The same analysis using the non-marginalized likelihood has been applied to Mock A



(a) $\Lambda = 0.15 h \text{ Mpc}^{-1}$.

(b) $\Lambda = 0.18 h \text{ Mpc}^{-1}$.



(c) $\Lambda = 0.2 h \text{ Mpc}^{-1}$.

Figure 11: Posterior of parameters for the inference performed on Mock A.

sampled with the Lagrangian bias. The results of this analysis are summarized in Fig. 15. Similarly as in the case of mock B, we find that the error bar $\sigma(\beta)$ is the same as when the marginalized likelihood is used for the same cutoff.

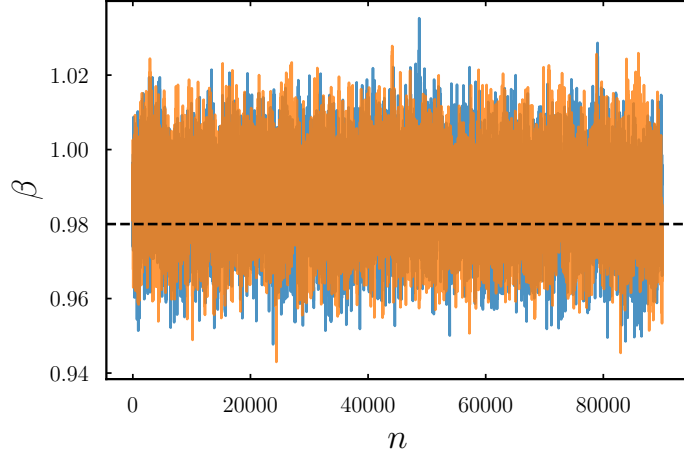


Figure 12: Trace plot for parameter β in chains generated using the non-marginalized likelihood. Inference was performed at $\Lambda = 0.15 h \text{ Mpc}^{-1}$ for Mock B.

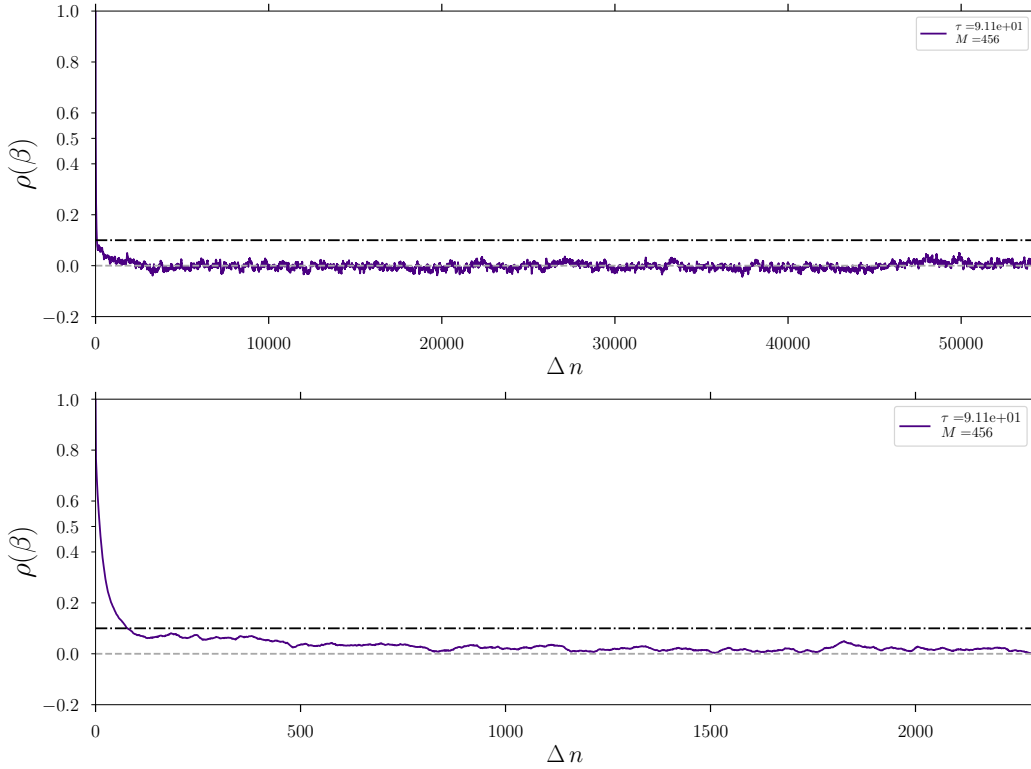


Figure 13: The normalized auto-correlation function for parameter β inferred at $\Lambda = 0.15 h \text{ Mpc}^{-1}$ using the non-marginalized likelihood. We also show the correlation length value τ together with the maximum separation M between the samples considered. The lower panel zooms in on the first 3000 samples.

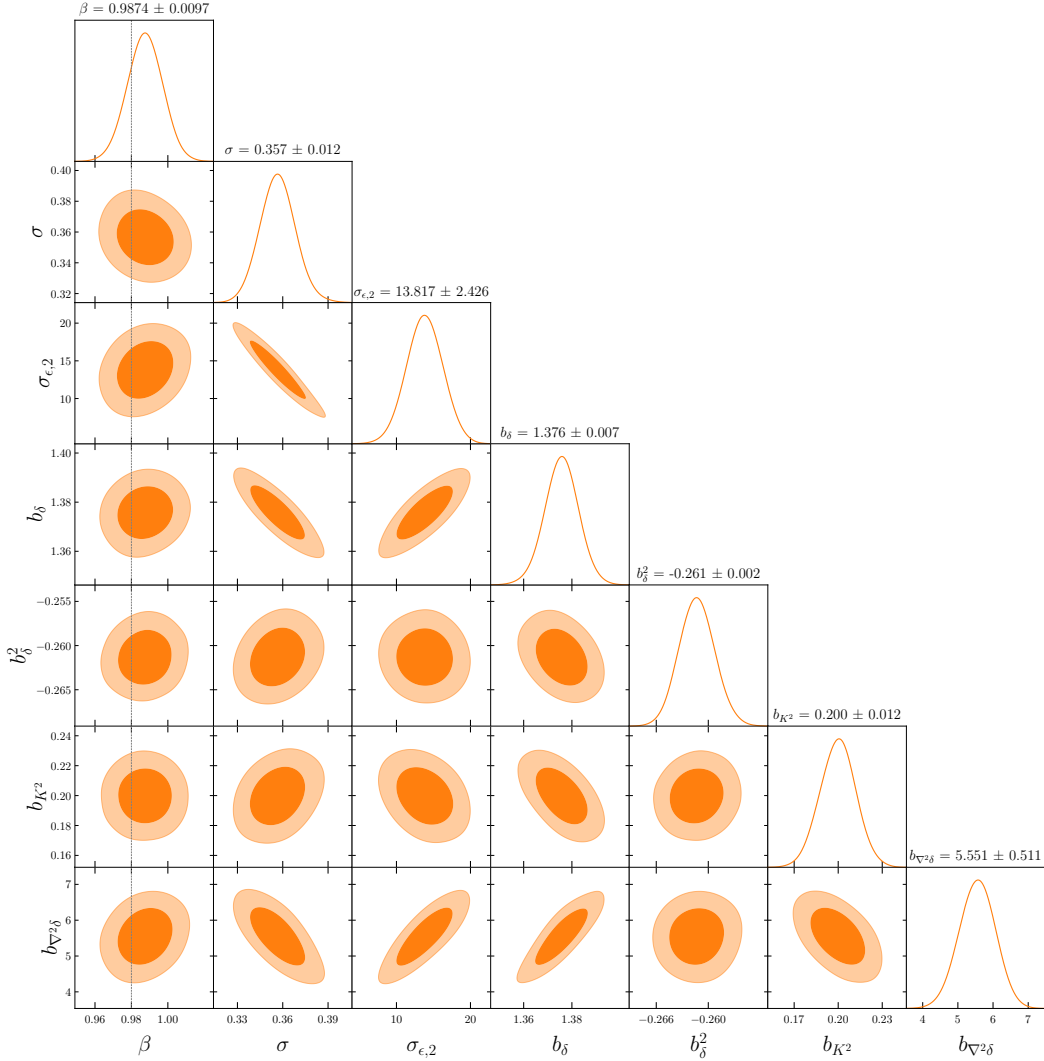


Figure 14: Results of the joint FreeIC inference on the Mock B using non-marginalized likelihood and Eulerian bias. We show the posterior for all noise parameters, bias parameters and β . Inference was performed at $\Lambda = 0.15 h \text{ Mpc}^{-1}$.

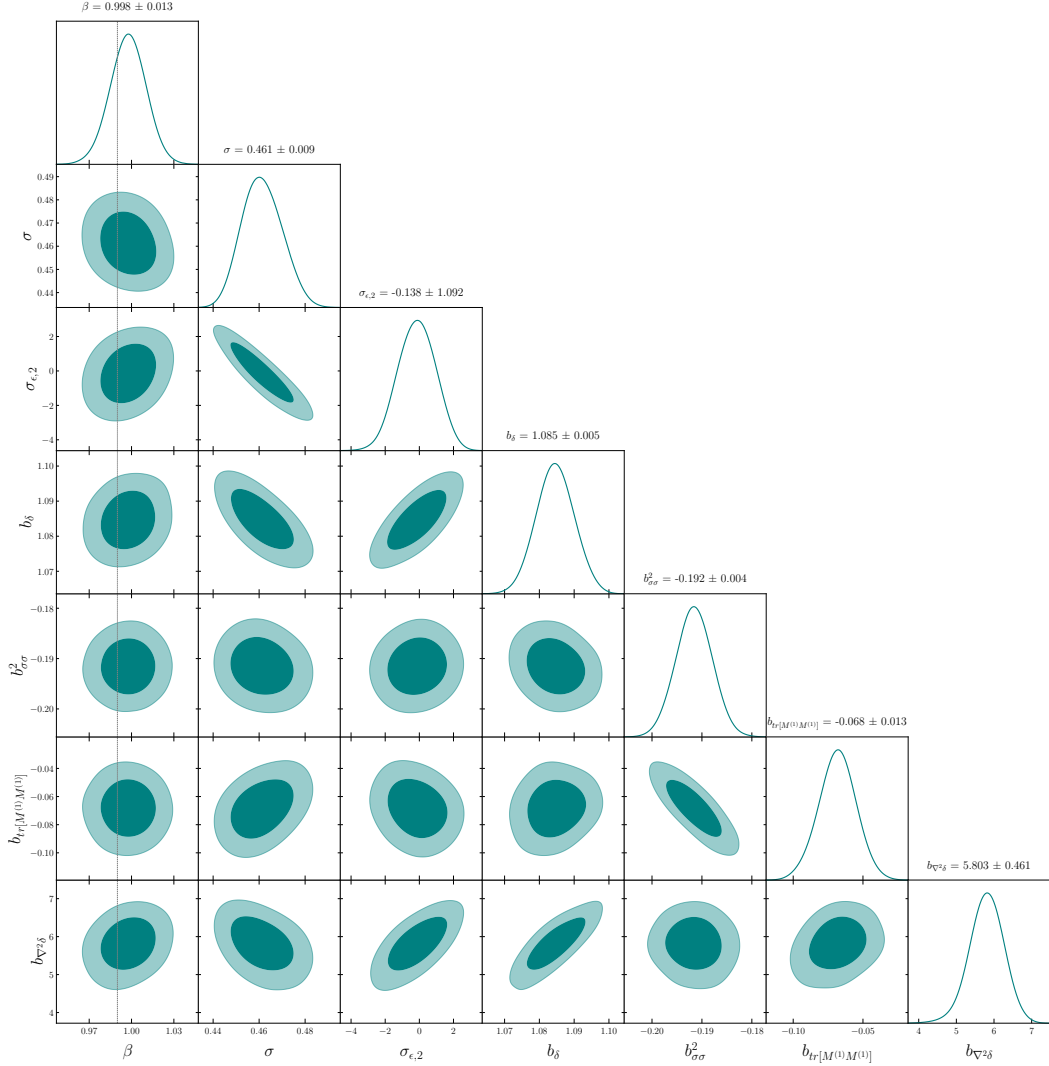


Figure 15: Results of the joint FreeIC inference on the Mock A using non-marginalized likelihood and Lagrangian bias. We show the posterior for all noise parameters, bias parameters and β . Inference was performed at $\Lambda = 0.15 h \text{ Mpc}^{-1}$.

References

- [1] Daniel J. Eisenstein, Hee-Jong Seo, and Martin White. On the robustness of the acoustic scale in the low-redshift clustering of matter. *The Astrophysical Journal*, 664(2):660–674, Aug 2007.
- [2] Hee-Jong Seo and Daniel J. Eisenstein. ”improved forecasts for the baryon acoustic oscillations and cosmological distance scale”. *The Astrophysical Journal*, 665(1):14–24, Aug 2007.
- [3] Nikhil Padmanabhan, Martin White, and J. D. Cohn. Reconstructing baryon oscillations: A Lagrangian theory perspective. *Phys. Rev. D*, 79(6):063523, March 2009.
- [4] Blake D. Sherwin and Matias Zaldarriaga. Shift of the baryon acoustic oscillation scale: A simple physical picture. *Phys. Rev. D*, 85(10):103523, May 2012.
- [5] Daniel J. Eisenstein, Hee-Jong Seo, Edwin Sirko, and David N. Spergel. Improving cosmological distance measurements by reconstruction of the baryon acoustic peak. *The Astrophysical Journal*, 664(2):675–679, August 2007.
- [6] Daniel J. Eisenstein, Hee-Jong Seo, and Martin White. On the robustness of the acoustic scale in the low-redshift clustering of matter. *The Astrophysical Journal*, 664(2):660–674, August 2007.
- [7] Nikhil Padmanabhan, Martin White, and J. D. Cohn. Reconstructing baryon oscillations: A lagrangian theory perspective. *Physical Review D*, 79(6), March 2009.
- [8] Yanlong Shi, Marius Cautun, and Baojiu Li. New method for initial density reconstruction. *Phys. Rev. D*, 97(2):023505, January 2018.
- [9] Yookyung Noh, Martin White, and Nikhil Padmanabhan. Reconstructing baryon oscillations. *Physical Review D*, 80(12), Dec 2009.
- [10] Svetlin Tassev and Matias Zaldarriaga. Towards an optimal reconstruction of baryon oscillations. *Journal of Cosmology and Astroparticle Physics*, 2012(10):006–006, Oct 2012.
- [11] A. Burden, W. J. Percival, and C. Howlett. Reconstruction in Fourier space. *Monthly Notices of the Royal Astronomical Society*, 453(1):456–468, Aug 2015.
- [12] Marcel Schmittfull, Yu Feng, Florian Beutler, Blake Sherwin, and Man Yat Chu. Eulerian BAO reconstructions and n -point statistics. *Phys. Rev. D*, 92:123522, Dec 2015.
- [13] Xin Wang, Hao-Ran Yu, Hong-Ming Zhu, Yu Yu, Qiaoyin Pan, and Ue-Li Pen. Isobaric Reconstruction of the Baryonic Acoustic Oscillation. *The Astrophysical Journal*, 841(2):L29, Jun 2017.
- [14] Marcel Schmittfull, Tobias Baldauf, and Matias Zaldarriaga. Iterative initial condition reconstruction. *Physical Review D*, 96(2), Jul 2017.
- [15] Fabian Schmidt, Franz Elsner, Jens Jasche, Nhat Minh Nguyen, and Guilhem Lavaux. A rigorous EFT-based forward model for large-scale structure. *Journal of Cosmology and Astroparticle Physics*, 2019(01):042–042, Jan 2019.
- [16] Ivana Babić, Fabian Schmidt, and Beatriz Tucci. BAO scale inference from biased tracers using the EFT likelihood. *Journal of Cosmology and Astroparticle Physics*, 2022(08):007, aug 2022.
- [17] Daniel Baumann, Alberto Nicolis, Leonardo Senatore, and Matias Zaldarriaga. Cosmological non-linearities as an effective fluid. *Journal of Cosmology and Astroparticle Physics*, 2012(07):051–051, Jul 2012.
- [18] John Joseph M. Carrasco, Mark P. Hertzberg, and Leonardo Senatore. The effective field theory of cosmological large scale structures. *Journal of High Energy Physics*, 2012(9), Sep 2012.

- [19] Franz Elsner, Fabian Schmidt, Jens Jasche, Guilhem Lavaux, and Nhat-Minh Nguyen. Cosmology inference from a biased density field using the EFT-based likelihood. *Journal of Cosmology and Astroparticle Physics*, 2020(01):029–029, Jan 2020.
- [20] Giovanni Cabass and Fabian Schmidt. The EFT likelihood for large-scale structure. *Journal of Cosmology and Astroparticle Physics*, 2020(04):042–042, Apr 2020.
- [21] Fabian Schmidt, Giovanni Cabass, Jens Jasche, and Guilhem Lavaux. Unbiased cosmology inference from biased tracers using the EFT likelihood. *Journal of Cosmology and Astroparticle Physics*, 2020(11):008–008, Nov 2020.
- [22] Fabian Schmidt. Sigma-eight at the percent level: the EFT likelihood in real space. *Journal of Cosmology and Astroparticle Physics*, 2021(04):032, Apr 2021.
- [23] Andrija Kostić, Nhat-Minh Nguyen, Fabian Schmidt, and Martin Reinecke. Consistency tests of field level inference with the eft likelihood. *Journal of Cosmology and Astroparticle Physics*, 2023(07):063, July 2023.
- [24] Nhat-Minh Nguyen, Fabian Schmidt, Beatriz Tucci, Martin Reinecke, and Andrija Kostić. How much information can be extracted from galaxy clustering at the field level?, 2024.
- [25] Julia Stadler, Fabian Schmidt, and Martin Reinecke. Cosmology inference at the field level from biased tracers in redshift-space. *Journal of Cosmology and Astroparticle Physics*, 2023(10):069, October 2023.
- [26] Jens Jasche and Francisco S. Kitaura. Fast Hamiltonian sampling for large-scale structure inference. *Monthly Notices of the Royal Astronomical Society*, 407(1):29–42, Jun 2010.
- [27] Radford Neal. MCMC Using Hamiltonian Dynamics. In *Handbook of Markov Chain Monte Carlo*, pages 113–162. 2011.
- [28] Radford M. Neal. Slice sampling, 2000.
- [29] Fabian Schmidt. An n-th order Lagrangian forward model for large-scale structure. *Journal of Cosmology and Astroparticle Physics*, 2021(04):033, Apr 2021.
- [30] Doogesh Kodi Ramanah, Guilhem Lavaux, Jens Jasche, and Benjamin D. Wandelt. Cosmological inference from Bayesian forward modelling of deep galaxy redshift surveys. *A&A*, 621:A69, January 2019.
- [31] Daniel J. Eisenstein, Hee-Jong Seo, Edwin Sirko, and David N. Spergel. Improving cosmological distance measurements by reconstruction of the baryon acoustic peak. *The Astrophysical Journal*, 664(2):675–679, August 2007.
- [32] Henrique Rubira and Fabian Schmidt. Galaxy bias renormalization group. *JCAP*, 2024(1):031, January 2024.
- [33] Julien Lesgourgues. The Cosmic Linear Anisotropy Solving System (CLASS) I: Overview, 2011.
- [34] Takahiko Matsubara. Resumming cosmological perturbations via the lagrangian picture: One-loop results in real space and in redshift space. *Physical Review D*, 77(6), mar 2008.
- [35] C. Rampf. The recursion relation in Lagrangian perturbation theory. *JCAP*, 12:4, December 2012.
- [36] Vladislav Zheligovsky and Uriel Frisch. Time-analyticity of lagrangian particle trajectories in ideal fluid flow. *Journal of Fluid Mechanics*, 749:404–430, may 2014.
- [37] Takahiko Matsubara. Recursive solutions of lagrangian perturbation theory. *Physical Review D*, 92(2), Jul 2015.
- [38] Donghui Jeong and Fabian Schmidt. Large-scale structure observables in general relativity. *Classical and Quantum Gravity*, 32(4):044001, jan 2015.

- [39] Vincent Desjacques, Donghui Jeong, and Fabian Schmidt. Large-scale galaxy bias. *Physics Reports*, 733:1–193, Feb 2018.
- [40] Mehrdad Mirbabayi, Fabian Schmidt, and Matias Zaldarriaga. Biased tracers and time evolution. *Journal of Cosmology and Astroparticle Physics*, 2015(07):030–030, Jul 2015.
- [41] Alex H. Barnett, Jeremy F. Magland, and Ludvig af Klinteberg. A parallel non-uniform fast fourier transform library based on an ”exponential of semicircle” kernel, 2019.
- [42] Julia Stadler, Fabian Schmidt, and Martin Reinecke. Fast, accurate and perturbative modeling of the cosmic large scale structure; part i: Tracer restframe. In preparation.
- [43] Titouan Lazeyras, Alexandre Barreira, and Fabian Schmidt. Assembly bias in quadratic bias parameters of dark matter halos from forward modeling. *JCAP*, 2021(10):063, October 2021.
- [44] Beyond-2pt Collaboration, :, Elisabeth Krause, Yosuke Kobayashi, Andrés N. Salcedo, Mikhail M. Ivanov, Tom Abel, Kazuyuki Akitsu, Raul E. Angulo, Giovanni Cabass, Sofia Contarini, Carolina Cuesta-Lazaro, ChangHoon Hahn, Nico Hamaus, Donghui Jeong, Chirag Modi, Nhat-Minh Nguyen, Takahiro Nishimichi, Enrique Paillas, Marcos Pellejero Ibañez, Oliver H. E. Philcox, Alice Pisani, Fabian Schmidt, Satoshi Tanaka, Giovanni Verza, Sihan Yuan, and Matteo Zennaro. A Parameter-Masked Mock Data Challenge for Beyond-Two-Point Galaxy Clustering Statistics. *arXiv e-prints*, page arXiv:2405.02252, May 2024.
- [45] Henrique Rubira and Fabian Schmidt. The Renormalization Group for Large-Scale Structure: Origin of Galaxy Stochasticity. *arXiv e-prints*, page arXiv:2404.16929, April 2024.
- [46] Beatriz Tucci and Fabian Schmidt. EFTofLSS meets simulation-based inference: σ_8 from biased tracers. *JCAP*, 2024(5):063, May 2024.
- [47] Alan D. Sokal. Monte carlo methods in statistical mechanics: Foundations and new algorithms note to the reader. 1996.